

Topology, Landscapes, and Biomolecular Energy Transport

Justin E. Elenewski,^{1,2} Kirill A. Velizhanin,³ and Michael Zwolak^{1,*}

¹*Biophysics Group, Microsystems and Nanotechnology Division, Physical Measurement Laboratory, National Institute of Standards and Technology, Gaithersburg, MD 20899, USA*

²*Maryland Nanocenter, University of Maryland, College Park, MD 20742, USA*

³*Theoretical Division, Los Alamos National Laboratory, Los Alamos, NM 87545 USA*

While ubiquitous, energy redistribution remains a poorly understood facet of the nonequilibrium thermodynamics of biomolecules. At the molecular level, finite-size effects, pronounced nonlinearities, and ballistic processes conspire to produce behavior that diverges from the macroscale. Here, we show that transient thermal transport reflects macromolecular energy landscape architecture through both (i) the topological characteristics of the conformational ensemble and (ii) the nonlinear processes that mediate dynamics. While the former determines transport pathways via molecular contacts, the latter reflects the ruggedness of the landscape for local motion of atoms and molecular fragments. Unlike transport through small-molecule systems, such as alkanes, nonlinearity dominates over coherent processes at even quite short time- and length-scales. Our exhaustive all-atom simulations and novel local-in-time and space analysis, applicable to both theory and experiment, permit dissection of energy migration in biomolecules. The approach demonstrates that vibrational energy transport can probe otherwise inaccessible aspects of macromolecular dynamics and interactions that underly biological function.

Biological systems are characterized by a persistent nonequilibrium state, maintained by the open metabolic reactions that drive self-replication. Directed redistribution of energy is an intrinsic feature, serving to generate mechanical motion [1, 2], mediate allosteric communication [3–5], and drive bioenergetic processes [6–8]. The physical scales of these processes can be surprising: Common enzymatic reactions liberate up to 2 eV of heat repeatedly over micro- to milli-second catalytic cycles [8]. This energy is redistributed throughout the surrounding protein scaffold within picoseconds and is either dissipated to mitigate thermally-induced stress, leveraged to induce mechanical motion, or employed to promote further catalytic activity. Irrespective of the endpoint, efficient and directed energy transport is critical to the function of these nanoscale machines.

At the macroscale, Fourier’s law, $J = -\kappa \nabla T$ and its time-dependent version capture the flow of heat, given by the flux J , in response to a temperature gradient ∇T . Those two quantities are related by the thermal conductivity κ (or the diffusivity D), which can be anisotropic.

This situation is more complicated at the nanoscale, where competing ballistic and diffusive transport pathways impede a universal description [9, 10]. We will show that, surprisingly, Fourier’s law captures the bulk of transient energy flow in a paradigmatic polypeptide, provided that one accounts for the fact that fluxes and diffusivities are temperature dependent. Departures from a simple realization of Fourier’s law happen at large temperature gradients, beyond about 15 K/residue, even though transport is still diffusive. The identification of these regimes is not possible through all-atom molecular dynamics alone [11–17] or normal-mode analysis (even when treating anharmonicity as a correction) [18–24]. The former does not unravel the atomic-scale mechanisms of transport and the latter reflects dynamics only at potential energy minima [21].

Despite the ubiquity of energy distribution and flow in biomolecular systems, experiments are difficult [6, 26–30]. In a pioneering work, Botan *et al.* developed an approach to monitor real-time heat migration in a polypeptide of 2-aminoisobutyric acid (Aib) [27]. The approach employs a photoexcitable azobenzene tag as a heater and backbone carbonyl modes as local vibrational thermometers. The results are complex, suggesting a ‘dynamical transition’ temperature above which transport is enhanced [31–34]. Quantum and nonequilibrium molecular dynamics (NEMD) simulations support the presence of a transition in transport properties, and also suggest that a classical description is realistic [12–15] (unlike for small molecules [35–39]). However, both the nature of the transition and mechanism of transport remain unclear, with theory giving conflicting accounts [12, 13, 27, 31, 40].

We use NEMD simulations as a starting point, since the lack of symmetries, granularity, and high-dimensional free energy landscapes of biomolecules make numerical simulations imperative [41–43]. Our simulation system is a ten-residue Aib helix (Aib₁₀ solvated by chloroform, similar to experimental efforts [27, 31–34]). We previously generated temperature-dependent free energy landscapes for Aib₁₀ at high resolution with replica-exchange simulations [25]. From the resulting conformational ensemble, we extract 4000 conformers for each environmental (bath) temperature T_B according to a Boltzmann distribution. This includes structures from both left- and right-handed folding funnels, ensuring a uniform distribution of configurations (Fig. 1a,b). We initiate NEMD simulations in a manner that mimics photoexcitation,

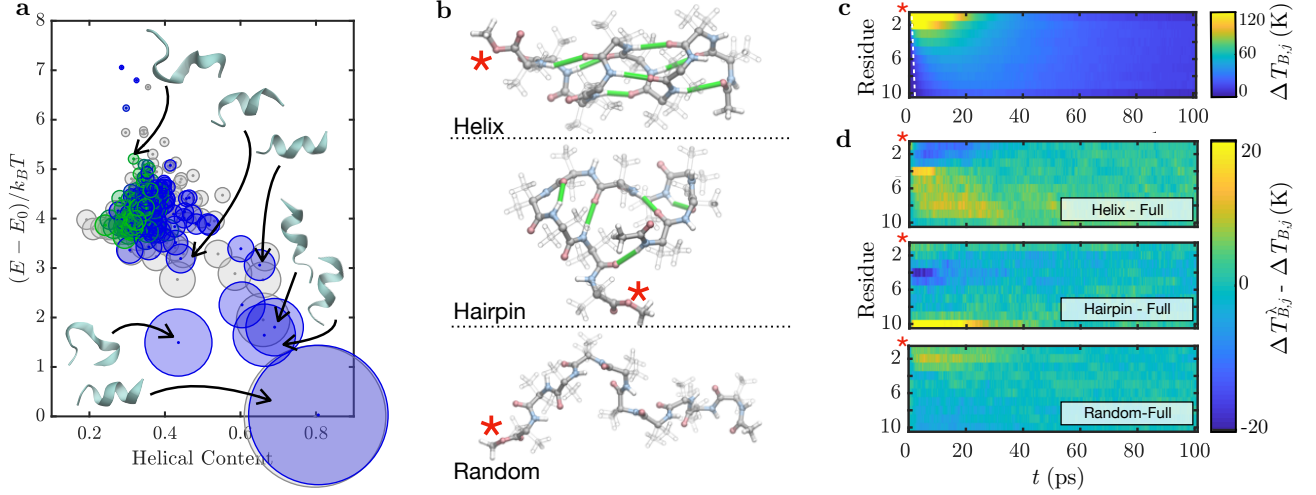


FIG. 1. Free energy landscape, topology, and energy transport. (a) Conformational clusters within the Aib₁₀ free energy landscape at the solvent bath temperature $T_B = 230.0$ K. The size of a data points reflect the relative population of a k -means structural cluster at 2.6 nm root-mean-square deviation (RMSD) cutoff. States for a right-handed helix are colored from blue (more chiral) to green (less chiral), while those of a left-handed helix are uniformly grey. Helicity parameters and ensemble determinations follow Ref. [25]; (b) Major conformers in the Aib₁₀ structural ensemble. The C-terminal heater residue is denoted by a red asterisk (*), and hydrogen bonds are colored green; (c) Thermal transport profile from NEMD simulations, characterized as a per-residue kinetic temperature elevation $\Delta T_{B,j}(t) = \langle T_j(t) \rangle - T_B$ with respect to the solvent bath. The dashed, white line demarcates the ballistic front; (d) Differential heat transport between a full structural ensemble and those ($\Delta T_{B,j}^\lambda$) containing only λ = helical, hairpin, or unstructured populations. Upper and lower temperature elevation (e.g., $\Delta T_{B,j}$) bounds are a cutoff for all values lying above or below the bound, respectively.

distributing ≈ 1.6 eV of energy between designated vibrational degrees of freedom in each conformer. This is achieved by thermostating the C-terminal residue to a temperature $T' = T_B + \Delta T$, with $\Delta T = 700$ K, while holding the remainder of the system at T_B . The simultaneous heating of all vibrational degrees of freedom in the heater residue is well-founded, as it yields thermal transport profiles that are indistinguishable from mode-selective heating [12, 27]. This excess energy then propagates freely within the microcanonical ensemble (i.e., without thermostating).

The conformational ensemble of Aib₁₀ comprises three general structural motifs (Fig. 1b) corresponding to (i) 3₁₀-/ α -helical conformers (≈ 45 % of ensemble) with hydrogen bonding between residue j and residue $j + 3$ or $j + 4$, respectively; (ii) hairpin-like configurations, with hydrogen bonds between the first and last residues of Aib₁₀ ($\approx 15\%$); and (iii) unstructured or extended conformers that have no consistent hydrogen bonding ($\approx 40\%$) [25]. We index these subensembles with λ . This partition is defined by the underlying free energy landscape, and is thus independent of our thermal transport simulations [25].

In Fig. 1c,d, we present transport profiles for Aib₁₀ versus the ensemble-averaged temperature elevation $\Delta T_{B,j}(t) = \langle T_j(t) \rangle - T_B$ of the j^{th} residue, or $\Delta T_{B,j}^\lambda - \Delta T_{B,j}$ for subensemble λ . The full-ensemble profile exhibits a weak thermal front that traverses the pep-

tide within 2 ps, apparent also in the helical ensemble (Fig. 1d). This corresponds to backbone propagation at $v = 1.7$ nm ps⁻¹, approaching ballistic transport velocities in biomolecular materials and alkyl chains [27, 36–38, 44]. While this channel is weak, additional ballistic pathways may exist at lower group velocities in different vibrational bands [44, 45], though these will inevitably be obscured by more prominent diffusive features. There is also rapid transport with both ballistic and diffusive characteristics across hydrogen-bonded regions, which can be seen in the helical and hairpin conformers (see discussion below).

While a ballistic pathway exists, the majority of energy transport is nonetheless diffusive — yielding a broad profile that is sensitive to both temperature and molecular conformation. We separate diffusive and ballistic behavior by coarse-graining in time (into 100 fs bins), averaging away signatures of very fast dynamics, but retain spatial coarse-graining into individual amino acid residues. We will develop time-dependent quantitative methods to extract diffusivities, free energies, and other characteristics from temperature-based data. However, to facilitate comparison with prior theory and experiment, we initially calculate diffusivities through the time to reach the maximal temperature for each residue. Considering just the helical subensemble for fitting, the temperature-dependent thermal diffusivity $D(T_B)$ has distinct low- and high-temperature regimes (Fig. 2a), which are also

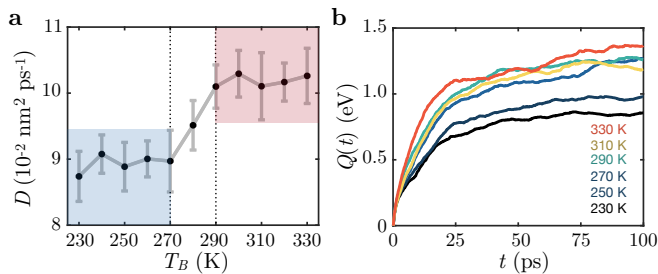


FIG. 2. **Benchmarks for thermal transport.** (a) Heat diffusivity D along the major axis of helical Aib₁₀ at increasing bath temperatures T_B . Diffusivities are derived from the time t_{\max} to reach the maximal temperature at each residue following a model $t_{\max} = d^2/D$, where d is the distance from the heater site. Colored regions denote low- (blue) and high-temperature (red) regimes (error bars are plus/minus one standard error). (b) Net heat $Q(t)$ transferred from residue two to three versus simulation time and bath temperature, following the scheme of Eq. (1). Error bands for the maximal cumulative integration error, as well as net heat transfer between other residues, are in the SI.

reflected in the net heat transfer (Fig. 2b). This behavior agrees with other experimental [27, 32, 34] and theoretical [12, 13, 27] efforts, which report diffusivities of $0.02 \text{ nm}^2 \text{ ps}^{-1}$ and $0.1 \text{ nm}^2 \text{ ps}^{-1}$, respectively. Theoretical $D(T_B)$ from this type of estimate consistently exceed experimental values for Aib₁₀ but are comparable to bulk materials [38] and other proteins [24]. Force-field parameterization likely contributes to this discrepancy. We will see, through an alternate analysis, that residual ballistic components also play a role. The crossover near 270 K is consistent with prior efforts, which ascribe this behavior to a glass-like dynamical transition [12, 27, 32, 34]. We will return to this point.

Given this diverse ensemble, it is natural to ask how transport behaves in different conformers. This question was not addressed by prior computational efforts, as they remained below the timescale for structural interconversion, sampling only helical configurations [12, 27]. Figure 1d shows the transport profile of the full Aib₁₀ ensemble compared to ensembles that contain only helical motifs, hairpin motifs, or randomly oriented conformers without fixed secondary structure. On a residue-by-residue basis, helical conformers propagate heat more readily than the full ensemble. This is evidenced by less energy retention at the heater site for $t \leq 25$ ps, commensurate with enhanced transfer to its hydrogen-bonded contacts at early times (mostly site 4 for the helix). The randomly oriented conformers transport heat less efficiently, underscored by enhanced energy localization at the first three residues for short times and, later, a rate of energy migration that lies slightly below the full ensemble. We expect a dominant backbone contribution in this case, as longer range contacts are sporadic. Hairpin configurations are intermediate with enhanced transport

to certain hydrogen bond contacts (site 10), in turn reducing the amount of heat transport through others (to the fourth site). It should be noted that, while hydrogen bonding can lead to more efficient heat transport for certain conformers, backbone channels always carry the majority of heat. Changes in energy migration are not due to local solvent heating, which raises the local bath temperature by at most 5 K over the entire simulation.

These observations indicate that topologically non-trivial configurations yield efficient pathways for vibrational energy migration. The importance of secondary and tertiary contacts has been previously invoked when describing transport within a single conformer of HP36 [17, 24]. We extend this observation, demonstrating that representative heat transport characteristics can be obtained only when the conformational landscape is comprehensively sampled. This is particularly important for metrologies, where insufficient sampling can lead to erroneous diffusivities and the misidentification of transport pathways. Moreover, changing conditions (temperature, pH, presence of denaturants, etc.) can shift the conformational ensemble, particularly near structural transitions. This will be detected by the energy transport, including the capture of additional information about underlying interactions [46, 47].

While molecular connectivity clearly determines transport pathways, NEMD simulations and existing analysis frameworks afford no immediate means to reconcile temperature-dependent features with microscopic processes and the underlying free energy landscape. To directly address this, we analyze the intermediate-timescale dynamics of NEMD trajectories – restricting to helical Aib₁₀ conformers for both structural heterogeneity and consistency with prior work – using a master equation for the kinetic energy E_j of the j^{th} residue in the peptide:

$$\begin{aligned} \dot{E}_j(t) = \sum_i [k_{ij}(t)E_i(t) - k_{ji}(t)E_j(t)] \\ - k_{s,j}(t)[E_{s,j}(t) - E_j(t)]. \end{aligned} \quad (1)$$

In this case, $k_{ij}(t)$ is a rate constant for energy transfer from residue i to residue j and $k_{ji}(t)$ is a distinct rate for the reverse process (see Methods), $k_{s,j}(t)$ is the rate of heat transfer to the solvent bath, and $E_{s,j}(t)$ is the kinetic energy density of the solvent surrounding the j^{th} residue (scaled to match the residue degrees of freedom). We diverge from earlier work by treating the $k_{ij}(t)$ as parameters that depend on both position and time – thereby implying a temperature dependence. This accommodation is key to our subsequent analysis. Given this arrangement, one can identify two distinct intra-peptide couplings: (i) direct transfer between nearest-neighbors in the peptide backbone ($k_{j,j+1}$ and $k_{j,j-1}$) and (ii) a long distance coupling between hydrogen bonding partners ($k_{j,j+3}$, $k_{j,j+4}$ for ideal 3₁₀- and α -helices,

respectively). With additional approximations, the system in Eq. (1) becomes well-posed and solvable at all times (see Methods). This diverges from existing master equation analyses which assume rate constants that are time-independent, and thus independent of the local temperatures and gradients [17].

Our remaining discussion is driven by the pairwise heat fluxes $J_{i,j}(t_n) = -k_{i,j}(t_n)[E_i(t_n) - (f_j/f_i)E_j(t_n)]$ and rate constants between coupled residues. Here f_j is the number of degrees of freedom for residue j and t_n indexes the time domain coarse-graining of the simulation trajectory into $n \leq N$ bins via block averaging. This approach is a finite difference decomposition of the diffusion equation $\dot{E}(x, t) = D \nabla^2 E(x, t)$ at the timescale $\Delta t = t_{n+1} - t_n$ and a length-scale Δx defined by the distance between adjacent residues. The fluxes come from the finite difference decomposition of $J(x, t) = -D \nabla E(x, t)$.

The rate constants $k_{i,j}(t_n) = D(t_n)/(\Delta x)^2$, in particular, capture biomolecular heat diffusivity $D(t_n)$ and give a metric for energy landscape fragility. This latter property is reflected by the local, activated conformational changes underlying transport $k_{i,j} = \Omega_{i,j} \exp[-\Delta G_{i,j}/k_B T]$, where $\Delta G_{i,j}$ is the free energy barrier between heat-accepting microstates and $(\Omega_{i,j})^{-1}$ is an effective timescale for free diffusion, influenced by both the protein and its environmental coupling. While each pair of microstates is characterized by a distinct $\Delta G_{i,j}$, these values evolve during heat transport — commensurate with changes in the free energy landscape.

We employ this kinetic approach with an intermediate timescale ($\Delta t = 100$ fs), long enough to average over most coherent motion but short enough not to obscure the evolution of energy in time. The distribution of backbone fluxes J_{BB} is parameterized by an effective temperature gradient $\Delta_{ij}T_{\text{eff}} = 2[E_i - (f_j/f_i)E_j]/3Nk_B$ between residues i and j , where the flux is incident on a residue containing N atoms. While transport is explicitly quantified through J_{BB} for simplicity, the effect of hydrogen bonding is present when fitting the backbone flux distribution at hydrogen bonding sites. The results are in Fig. 3a.

Region A: The forward flux J_{BB} has a linear region for small $\Delta_{ij}T_{\text{eff}}$ (less than about 12 K), although it does not go to zero at $\Delta_{ij}T_{\text{eff}} = 0$. Purely diffusive transport will not afford a heat flux in the absence of a local temperature gradient. Thus, a finite J_{BB} at $\Delta_{ij}T_{\text{eff}} = 0$ may be a signature of ballistic/coherent behavior. Supporting this interpretation, we find that the zero-gradient flux to decrease with increasing Δt during coarse-graining, while only exhibiting small error bands at all scales (thus it is not due to short-timescale fluctuations). A linear fit to this regime gives an effective diffusivity of $D_{\text{eff,A}} = 2.3 \times 10^{-2} \text{ nm}^2 \text{ ps}^{-1}$ (or conductivity $\kappa_{\text{eff,A}} = 3.9 \times 10^{-3} \text{ eV K}^{-1} \text{ ps}^{-1}$). Fitting for small $\Delta_{ij}T_{\text{eff}}$, while ignoring the residual ballistic contribution

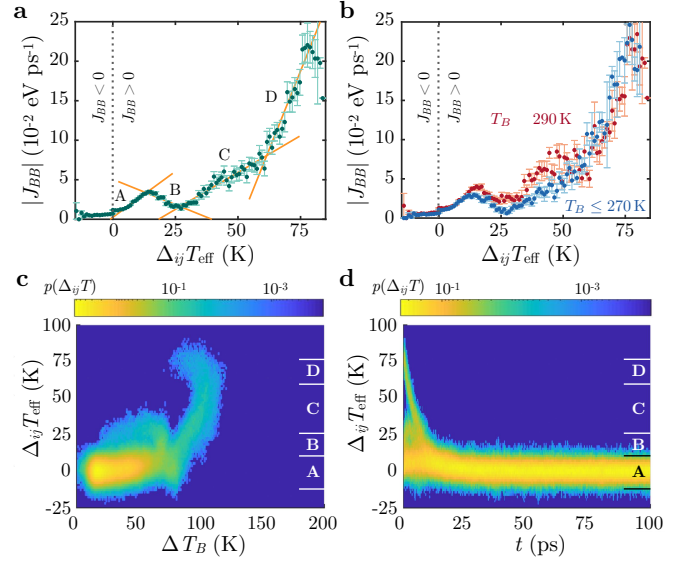


FIG. 3. Flux and thermal gradient distributions. (a) Backbone flux distributions (J_{BB}) for helical Aib₁₀ conformers. Fluxes are parameterized by the effective temperature gradient $\Delta_{ij}T_{\text{eff}}$ between adjacent residues, and a positive flux corresponds to flow away from the heater along the backbone. Transport regimes are labeled parallel to the text (A through D) and with orange lines for visibility. (b) The J_{BB} distribution may be partitioned into low-temperature (blue; 230 K to 270 K) and high-temperature (red; 290 K to 330 K) regimes. (c) Distribution of local temperature gradients $\Delta_{ij}T_{\text{eff}}$ versus average elevation $\Delta T_{B,j}(t) = \langle T_j(t) \rangle - T_B$ over the bath temperature and (d) versus simulation time t for the ensemble of MD trajectories. Labels (A–D) correspond to the regimes described in the text. Time series data from MD simulation is averaged with $\Delta t = 100$ fs for fits to the master equation, Eq. (1), and the resulting fluxes are block averaged in 1.0 K bins. The error bars are plus/minus one standard error.

right around $\Delta_{ij}T_{\text{eff}} = 0$, removes high rate constant artifacts. Encouragingly, the magnitude of the resulting diffusivity is consistent with experimental values. Employing the time to reach the maximum temperature, as done in prior theoretical work (see discussion above), affords much higher diffusivities. This linear regime has the same slope regardless of whether the lattice is in the low- or high-temperature regime (Fig. 3b).

The lack of a dependence on temperature indicates that this regime of transport occurs in a lightly corrugated landscape. In this case, the characteristic barrier scale is below 15 meV, and thus the mean energy at the lowest background temperature ($T_B = 230$ K) is above the corrugation. Lower temperature observations are necessary to identify the precise scale, requiring an accurate treatment of quantum effects and different experimental protocols. Stated more succinctly, the equality of the low- and high-temperature diffusivity indicates that the characteristic time Ω^{-1} is the same and no free energy barrier exists at this level of landscape hierarchy.

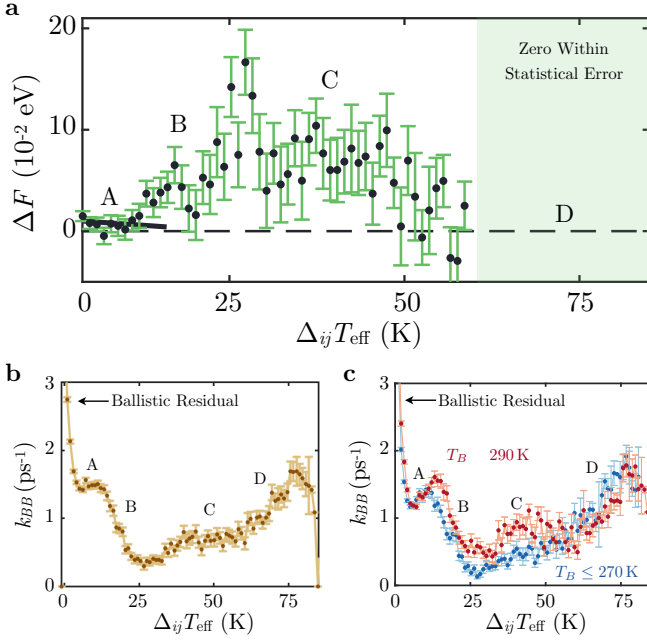


FIG. 4. **Thermal transport barriers and kinetic parameters.** (a) Effective free energy barriers ΔF corresponding to different regions of the J_{BB} flux profile. (b) Backbone rate distributions (k_{BB}) for helical Aib₁₀ conformers. Rate constants are parameterized by the temperature gradient $\Delta_{ij}T_{\text{eff}}$ between adjacent residues and (c) partitioned into low-temperature (blue; 230 K to 270 K) and high-temperature (red; 290 K to 330 K) regimes. The error bars are plus/minus one standard error.

Region B: As $\Delta_{ij}T_{\text{eff}}$ goes above 12 K, the flux decreases with the increasing temperature gradient. This suggests the appearance of a vibrational mismatch between adjacent residues due to nonlinearity. As a consequence, the molecular conformation is pushed into an activated region of the free energy landscape where the energy barrier is larger than the available kinetic energy and increases with $\Delta_{ij}T_{\text{eff}}$. Moreover, the average temperature elevation does not substantially change for $\Delta_{ij}T_{\text{eff}}$ in region B where the flux dips (Fig. 3c). Thus, barrier crossing is not aided by energy remaining from the initial deposition. This is further supported by the separation of low- and high-temperature curves, indicating that transport increases with temperature — a signature of a free energy barrier. The characteristic barriers can be estimated from the ratio of high- and low-temperature fluxes (or rates), $J_H/J_L \approx 1.2 \approx \exp(-\Delta F/k_B T_H + \Delta F/k_B T_L)$, giving values of ΔF that span from 28 meV to 167 meV when we use the average temperature in each regime (i.e., $T_L = 250$ K and $T_H = 310$ K).

Region C: As $\Delta_{ij}T_{\text{eff}}$ increases beyond 30 K, there is a substantial increase in flux for both low- and high-temperature structures. In this case, a large $\Delta_{ij}T_{\text{eff}}$ implies a larger average temperature elevation for a given

residue pair (Fig. 3c), as large gradients are primarily found at early times (and near the heater site) when a substantial fraction of initially deposited energy is present (Fig. 3d). If we assume Ω remains the same, the temperature elevation $\Delta T_{B,j}$ is enough to once again put transport in a stable regime of the landscape at this level of hierarchy, with a typical barrier energy of 67 meV. This yields an approximately linear region for J_{BB} with a diffusivity $D_{\text{eff},C} = 1.9 \times 10^{-2} \text{ nm}^2 \text{ ps}^{-1}$ ($\kappa_{\text{eff},C} = 3.2 \times 10^{-3} \text{ eV K}^{-1} \text{ ps}^{-1}$).

Region D: Increasing $\Delta_{ij}T_{\text{eff}}$ even further, beyond 50 K, leads to a new transport region with a larger diffusivity $D_{\text{eff},D} = 8.0 \times 10^{-2} \text{ nm}^2 \text{ ps}^{-1}$ ($\kappa_{\text{eff},D} = 1.3 \times 10^{-2} \text{ eV K}^{-1} \text{ ps}^{-1}$), corresponding to over-the-barrier diffusion. In this case, new landscape features become accessible, which would otherwise require strong activation at lower energies.

Figure 4a shows the effective free energy barriers in the different regimes, which are also reflected in the backbone rate constants (Fig. 4b,c). The k_{BB} initially decrease with $\Delta_{ij}T_{\text{eff}}$ (from 0 K to 4 K) due to a diminishing residual ballistic component (when averaging at $\Delta t = 100$ fs). This is followed by a plateau in k_{BB} at about 1.5 ps^{-1} between 4 K to 12 K, followed by a drop as the landscape is pushed into a new, barrier-dominated region. After this, though, the larger $\Delta_{ij}T_{\text{eff}}$ correspond to a larger temperature elevation, bringing the events above the features in the energy landscape and raising k_{BB} further. Our methods extract the dependence on the local temperature gradients (shown) and temperature elevation (not shown). Beyond $\Delta_{ij}T_{\text{eff}} = 77$ K, the rate constants and fluxes decline sharply, reflecting very early dynamics where strong dynamical localization processes dominate.

Finally, while our NEMD simulations support that a transition [12, 27, 32, 34] in diffusivity is present, they do not support that the transition happens solely due to the existence of energy barriers, as stated in Ref. [13, 27, 31], or glassy dynamics (which is certainly the case but does not pinpoint the particular processes that occur here). Rather, the transition is due to the development of region C physics: Energy flow, which largely happens from 0 to 10 ps, is in the presence of large $\Delta_{ij}T_{\text{eff}}$ (see initial time, high gradient line in Fig. 3d) on top of equilibrium fluctuations ($\Delta_{ij}T_{\text{eff}} \approx \pm 10$ K). We interpret this to indicate that large gradients give a vibrational mismatch via *nonlinear energy localization*, introducing a barrier to energy transport. In this context, localization would then mediate the transition into a higher diffusivity regime — thereby suggesting an origin of the sharpness of the transition. The increase of the base temperature reduces the vibrational mismatch by pushing the dynamics onto a different level of the landscape hierarchy. Simultaneous Arrhenius activation and barrier reduction conspire to give a sharp transition. More extensive simulations are necessary to make this precise.

These findings demonstrate that energy transport gives quantitative information regarding the biomolecular free energy landscape, its nonlinearity, and overall connectivity. Going beyond what we present here, the experimental analogues of our simulations offer potential probes of structural transitions, where a temperature-dependent change in the transport profile is a manifestation of the topology and nonlinear interactions of the dominant conformer(s). In other words, thermal transport can be employed to devise ‘tomographies’ that provide a complementary mapping of biomolecular structure, conformational dynamics, and folding pathways. Such probes might excel for highly fluctuating systems such as intrinsically disordered proteins (IDPs) or as a means to dissect local shifts in vibrational mode structure during molecular signaling or allostery. These dynamics have been impervious to other spectroscopies. Our approach provides the conceptual foundations and analysis tools that are directly applicable to experimental data, permitting the immediate interpretation of measurements that leverage local vibrational thermometry. In addition to the functional implications, the approach will also enable the development of a better understanding of what interactions look like at the atomic scale, and therefore better force-fields, and facilitate the design of nanodevices with directed, environmentally responsive heat transport mechanisms.

Acknowledgements

The authors would like to thank Thomas LeBrun for his insightful comments regarding this work. J. E. E. acknowledges support under the Cooperative Research Agreement between the University of Maryland and the National Institute for Standards and Technology Physical Measurement Laboratory, Award 70NANB14H209, through the University of Maryland. K. A. V. was supported by the U.S. Department of Energy through the LANL/LDRD Program. Computing resources were made available through the Los Alamos National Laboratory Institutional Computing Program, which is supported by the U.S. DOE National Nuclear Security Administration under contract no. DE-AC52-06NA25396, as well as the Maryland Advanced Research Computing Center (MARCC).

Methods

Molecular Dynamics Simulations. Our simulations consist of a modified Aib₁₀ peptide (AcOHN-Aib₁₀-COOCH₃), embedded in a box of 922 chloroform molecules. Equilibration and ensemble generation are described in Ref. [25]. Prior to NEMD runs, structures are further equilibrated for 100 ps at each base (T_B) temperature (NPT; time step $\delta t = 1.0$ fs) followed by a 50 ps run with shorter time step (NPT; $\delta t = 0.1$ fs). Using the final configurations, NEMD (NVT; $\delta t = 0.1$ fs) is initiated by heating the first residue of Aib₁₀ to $T_B + \Delta T$ ($\Delta T = 670$ K) for 1 ps, while holding the remaining

atoms at T_B . Thermostatting is then disabled and heat propagation monitored in the microcanonical ensemble. NVT simulations employ a velocity Verlet integrator and modified Nosé–Hoover thermostat (damping = 100 fs), while NPT runs add a Martyna–Tobias–Klein barostat (damping = 1000 fs, eight member chain) [48–50]. Isotropic cell fluctuations are allowed for NPT runs and initial velocities are assigned according to a Gaussian distribution. Simulations employ CHARMM36 force field parameters [51, 52], CHARMM pair potentials (without CMAP parameters, as rationalized in Ref. [25]), PPPM electrostatics (force cutoff 6.95×10^{-3} pN; pair coupling rescaled at 1.0 nm, terminated at 1.35 nm) and the LAMMPS codebase [53].

Kinetic Fitting. While physically descriptive, the master equation, Eq. (1), is underdetermined when fitting the simulated transport profiles $E_j(t) = 3/2N_jk_B\langle T(t) \rangle$ for the N_j atoms of the j^{th} residue. As a simplifying approximation, we relate forward and reverse rate constants $k_{ij} = (f_i/f_j)k_{ji}$ through the degrees of freedom of each residue f_j , as required for detailed balance to hold at equilibrium. We also restrict analysis to structurally homogeneous (helical) conformers, where the rate constants for hydrogen bond energy transfer $k_{j,j+3} \approx k_{j,j+4} \approx k_{HB}$ and solvent coupling $k_{s,j} \approx R_j k_s$ as are uniform quantities (up to a fixed geometric factor R_j for the surface area of terminal residues). Under these conditions, we may fit the time dependence of the solvent $k_s \rightarrow k_s(t)$ and peptide rate constants, $k_{ij} \rightarrow k_{ij}(t)$ and $k_{HB} \rightarrow k_{HB}(t)$, to account for the local temperature (which changes in time). This is in contrast to prior efforts that assume a uniform and time-independent backbone rate constant $k_{j,j+1} = k_{BB}$ [17].

Rate constants $\mathbf{k}_j = (k_{1,2}, \dots, k_{N-1,N}, k_H)$ at the n^{th} simulation time step are estimated for the linear system of Eq. (1) through a constrained optimization

$$\mathbf{k}(t_n) = \min_{\mathbf{k} \geq 0} \frac{1}{2} \|\mathbf{G}(t_n) \cdot \mathbf{k} - \mathbf{d}(t_n)\|^2 \quad (2)$$

where $\mathbf{d}_j(t_n) = [E_j(t_n) - E_j(t_{n-1})] + k_s(t_n)[E_j(t_n) - E_s]$ captures energy redistribution among residues of the peptide. The matrix $\mathbf{G}(t)$ is similarly defined so that $\mathbf{G}_{i,j}(t) = -\mathbf{G}_{i+1,j}(t) = -[E_i(t) - E_j(t)]$ accommodates backbone energy transport and $\mathbf{G}_{i,N}(t) = \sum_{\ell} [E_i - E_{\ell}]$ describes its hydrogen bonding counterpart to the i^{th} residue. The solvent coupling rate $k_s(t_n) = \sum_j [E_j(t_n) - E_j(t_{n-1})]/[E_j(t_n) - E_s(t_n)]$ is then given by the energy exchanged between the peptide and the solvent at each time step (the solvent bath energy $E_s(t_n) = 3N_jk_BT_B/2$ is treated a constant).

* mpz@nist.gov

- [1] Andrieux, D. & Gaspard, P. Fluctuation theorems and nonequilibrium thermodynamics of molecular motors. *Phys. Rev. E* **74**, 011906 (2006).
- [2] Hwang, W. & Hyeon, C. Quantifying the Heat Dissipation from a Molecular Motor's Transport Properties in Nonequilibrium Steady States. *J. Phys. Chem. Lett.* **8**, 250–256 (2017).
- [3] Tu, Y. The nonequilibrium mechanism for ultrasensitivity in a biological switch: Sensing by Maxwell's demons. *Proc. Nat. Acad. Sci. U. S. A.* **105**, 11737 (2008).
- [4] Wang, F. *et al.* Non-equilibrium effects in the allosteric regulation of the bacterial flagellar switch. *Nat. Phys.* **13**, 710–714 (2017).
- [5] Buchenberg, S., Sittel, F. & Stock, G. Time-resolved observation of protein allosteric communication. *Proc. Nat. Acad. Sci. U. S. A.* **114**, E6804–E6811 (2017).
- [6] Ansari, A. *et al.* Protein states and proteinquakes. *Proc. Nat. Acad. Sci. U. S. A.* **82**, 5000–5004 (1985).
- [7] Nedergaard, J., Ricquier, D. & Kozak, L. P. Uncoupling proteins: Current status and therapeutic prospects. *EMBO Rep.* **6**, 917–921 (2005).
- [8] Reidel, C. *et al.* The heat released during catalytic turnover enhances the diffusion of an enzyme. *Nature* **517**, 227–230 (2015).
- [9] Cahill, D. G. Nanoscale thermal transport. *J. Appl. Phys.* **93**, 793 (2003).
- [10] Cahill, D. G. *et al.* Nanoscale thermal transport. II. 2003–2013. *Appl. Phys. Rev.* **1**, 011305 (2014).
- [11] Nguyen, P. H., Derreumaux, P. & Stock, G. Energy Flow and Long-Range Correlations in Guanine-Binding Riboswitch: A Nonequilibrium Molecular Dynamics Study. *J. Phys. Chem. B* **113**, 9340–9347 (2009).
- [12] Nguyen, P. H., Park, S.-M. & Stock, G. Nonequilibrium molecular dynamics simulations of energy transport through a peptide helix. *J. Chem. Phys.* **132**, 025102 (2010).
- [13] Kobus, M., Nguyen, P. H. & Stock, G. Infrared signatures of the peptide dynamical transition: A molecular dynamics simulation study. *J. Chem. Phys.* **133**, 034512 (2010).
- [14] Kobus, M., Nguyen, P. H. & Stock, G. Coherent vibrational energy transfer along a peptide helix. *J. Chem. Phys.* **134**, 124518 (2011).
- [15] Goj, A. & Bittner, E. R. Mixed quantum-classical simulations of excitons in peptide helices. *J. Chem. Phys.* **134**, 205103 (2011).
- [16] Brinkmann, L. U. L. & Hub, J. S. Ultrafast anisotropic protein quake propagation after CO photodissociation in myoglobin. *Proc. Nat. Acad. Sci. U. S. A.* **113**, 10565–10570 (2016).
- [17] Buchenberg, S., Leitner, D. M. & Stock, G. Scaling Rules for Vibrational Energy Transport in Globular Proteins. *J. Phys. Chem. Lett.* **7**, 25–30 (2016).
- [18] Leitner, D. M. Vibrational Energy Transfer in Helices. *Phys. Rev. Lett.* **87**, 188102 (2001).
- [19] Yu, X. & Leitner, D. M. Vibrational Energy Transfer and Heat Conduction in a Protein. *J. Phys. Chem. B* **107**, 1698–1707 (2003).
- [20] Yu, X. & Leitner, D. M. Anomalous diffusion of vibrational energy in proteins. *J. Chem. Phys.* **119**, 12673 (2003).
- [21] Yu, X. & Leitner, D. M. Heat flow in proteins: Computation of thermal transport coefficients. *J. Chem. Phys.* **122**, 054902 (2004).
- [22] Leitner, D. M. Frequency-resolved communication maps for proteins and other nanoscale materials. *J. Chem. Phys.* **130**, 195101 (2009).
- [23] Gnanasekaran, R., Agbo, J. K. & Leitner, D. M. Communication maps computed for homodimeric hemoglobin: Computational study of water-mediated energy transport in proteins. *J. Chem. Phys.* **135**, 065103 (2011).
- [24] Leitner, D. M., Buchenberg, S., Brettel, P. & Stock, G. Vibrational energy flow in the villin headpiece subdomain: Master equation simulations. *J. Chem. Phys.* **142**, 075101 (2015).
- [25] Elenewski, J. E., Velizhanin, K. A. & Zwolak, M. A Spin-1 Representation for Dual-Funnel Energy Landscapes. *J. Chem. Phys.* **149**, 035101 (2018).
- [26] Šrajcar, V. *et al.* Photolysis of the Carbon Monoxide Complex of Myoglobin: Nanosecond Time-Resolved Crystallography. *Science* **274**, 1726–1729 (1996).
- [27] Botan, V. *et al.* Energy transport in peptide helices. *Proc. Nat. Acad. Sci. U. S. A.* **104**, 12749–12754 (2007).
- [28] Helbing, J. *et al.* Temperature Dependence of the Heat Diffusivity of Proteins. *J. Phys. Chem. A* **116**, 2620–2628 (2012).
- [29] Barends, T. R. M. *et al.* Direct observation of ultrafast collective motions in CO myoglobin upon ligand dissociation. *Science* **350**, 445–450 (2015).
- [30] Levantino, M. *et al.* Ultrafast myoglobin structural dynamics observed with an X-ray free-electron laser. *Nature Comm.* **6**, 6772 (2015).
- [31] Backus, E. H. G. *et al.* Energy Transport in Peptide Helices: A Comparison between High- and Low-Energy Excitations. *J. Phys. Chem. B* **112**, 9091–9099 (2008).
- [32] Backus, E. H. G. *et al.* Structural Flexibility of a Helical Peptide Regulates Vibrational Energy Transport Properties. *J. Phys. Chem. B* **112**, 15487–15492 (2008).
- [33] Schade, M., Moretto, A., Crisma, M., Toniolo, C. & Hamm, P. Vibrational Energy Transport in Peptide Helices after Excitation of C–D Modes in Leu-d10. *J. Phys. Chem. B* **113**, 13393–13397 (2009).
- [34] Backus, E. H. G. *et al.* Dynamical Transition in a Small Helical Peptide and Its Implication for Vibrational Energy Transport. *J. Phys. Chem. B* **113**, 13405–13409 (2009).
- [35] Wang, Z. *et al.* Ultrafast Flash Thermal Conductance of Molecular Chains. *Science* **317**, 787 (2007).
- [36] Rubtsova, N. I. *et al.* Room-temperature ballistic energy transport in molecules with repeating units. *J. Chem. Phys.* **142**, 212412 (2015).
- [37] Quasim, L. N. *et al.* Ballistic Transport of Vibrational Energy through and Amide Group Bridging Alkyl Chains. *J. Phys. Chem. C* **123**, 3381 (2019).
- [38] Rubtsov, I. V. & Burin, A. L. Ballistic and diffusive vibrational energy transport in molecules. *J. Chem. Phys.* **150**, 020901 (2019).
- [39] Liu, M., Kawauchi, T., Iyoda, T. & Piotrowiak, P. Vibrational Cooling in Oligomeric Viologens of Different Sizes and Topologies. *J. Phys. Chem. B* **123**, 1847–1854 (2019).
- [40] Schade, M. & Hamm, P. Vibrational energy transport in the presence of intrasite vibrational energy redistribution. *J. Chem. Phys.* **131**, 044511 (2009).
- [41] Wales, D. J., Miller, M. A. & Walsh, T. R. Archetypal energy landscapes. *Nature* **394**, 758–760 (1998).
- [42] Wales, D. J. & Bogdan, T. V. Potential Energy and Free

- Energy Landscapes. *J. Phys. Chem. B* **110**, 20765–20776 (2006).
- [43] Wales, D. J. Insight into reaction coordinates and dynamics from the potential energy landscape. *J. Chem. Phys.* **142**, 130901 (2015).
 - [44] Yue, Y. *et al.* Band-Selective Ballistic Energy Transport in Alkane Oligomers: Toward Controlling the Transport Speed. *J. Phys. Chem. B* **119**, 6448 (2015).
 - [45] Quasim, L. N. *et al.* Energy Transport in PEG Oligomers: Contributions of Different Optical Bands. *J. Phys. Chem. C* **120**, 26663 (2016).
 - [46] Velizhanin, K. A., Chien, C. C., Dubi, Y. & Zwolak, M. Driving denaturation: Nanoscale thermal transport as a probe of DNA melting. *Phys. Rev. E* **83**, 050906 (2011).
 - [47] Chien, C. C., Velizhanin, K. A., Dubi, Y. & Zwolak, M. Tunable Thermal Switching via DNA-Based Nano Devices. *Nanotechnology* **34**, 095704 (2013).
 - [48] Parrinello, M. & Rahman, A. Polymorphic transitions in single crystals: A new molecular dynamics method. *J. Appl. Phys.* **52**, 7182 (1981).
 - [49] Martyna, G. J., Tobias, D. J. & Klein, M. L. Constant pressure molecular dynamics algorithms. *J. Chem. Phys.* **101**, 4177–4189 (1994).
 - [50] Shinoda, W., Shiga, M. & Mikami, M. Rapid estimation of elastic constants by molecular dynamics simulation under constant stress. *Phys. Rev. B* **69**, 134103 (2004).
 - [51] MacKerell Jr., A. D., Feig, M. & Brooks, III, C. L. Improved Treatment of the Protein Backbone in Empirical Force Fields. *J. Am. Chem. Soc.* **126**, 698–699 (2004).
 - [52] Best, R. B. *et al.* Optimization of the additive CHARMM all-atom protein force field targeting improved sampling of the backbone phi, psi and side-chain chi1 and chi2 dihedral angles. *J. Chem. Theory Comput.* **8**, 3257–3273 (2012).
 - [53] Plimpton, S. Fast Parallel Algorithms for Short-Range Molecular Dynamics. *J. Comp. Phys.* **117**, 1–19 (1995).

Supplementary Information for
“Topology, Landscapes, and Biomolecular Energy Transport”

Justin E. Elenewski,^{1,2} Kirill A. Velizhanin,³ Michael Zwolak¹

¹*Biophysics Group, Microsystems and Nanotechnology Division, Physical Measurement
Laboratory, National Institute of Standards and Technology, Gaithersburg, MD, USA*

²*Maryland Nanocenter, University of Maryland, College Park, MD, USA*

³*Theoretical Division, Los Alamos National Laboratory, Los Alamos, NM, USA*

CONTENTS

I. Validation of Fitting Methods	2
II. Cumulative Heat Transfer: Bath Temperature Dependence	5
III. Hydrogen Bond Transport: Flux Distribution	14
IV. Distribution of Effective Backbone Gradients ($\Delta_{ij}T_{\text{eff}}$)	15
V. Heat Diffusivity and Master Equation Analysis	16

I. VALIDATION OF FITTING METHODS

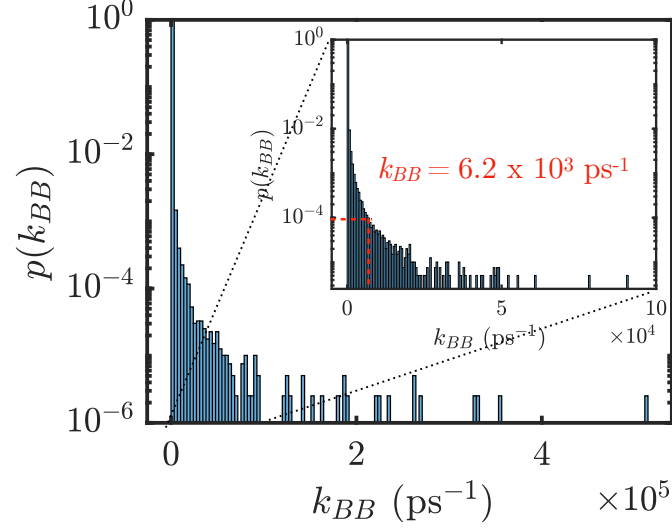


FIG. S1. **Rate constant distribution.** Probability density distribution $p(k_{BB})$ for backbone rate constants k_{BB} , as obtained using the master equation-based fitting method (Eq. 1 of the parent manuscript). Physically extremal values, defined as rates that exceed $6.2 \times 10^3 \text{ ps}^{-1}$, have a statistical weight of less than 1.0×10^{-4} , attesting to the robustness of the fitting algorithm. The distribution is presented as an aggregate for helical conformers at all temperatures, with simulation time series data coarse grained over $\Delta t = 100 \text{ fs}$ intervals prior to analysis.

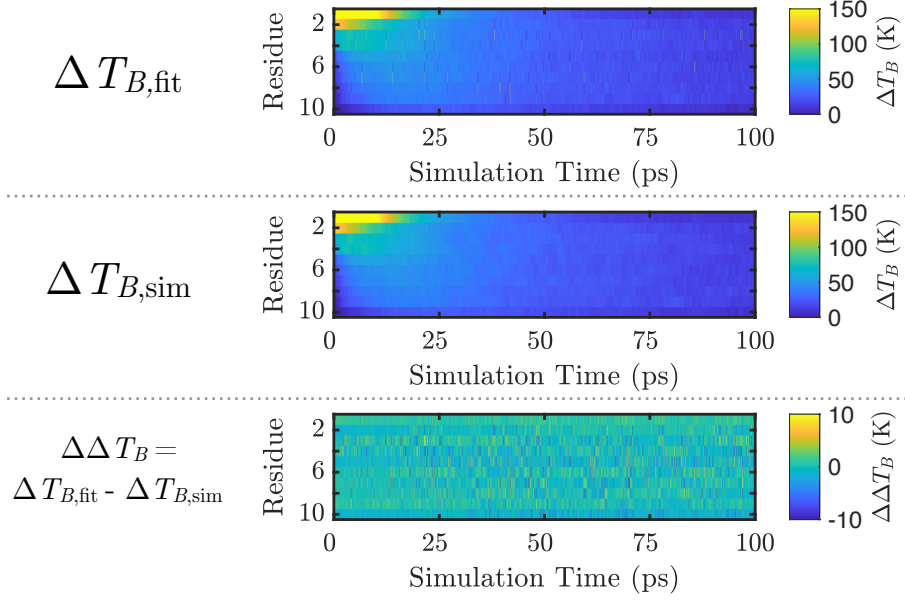


FIG. S2. **Reconstructed thermal transport profiles.** To demonstrate robustness of our master equation reconstruction (Eq. 1 of the manuscript), molecular dynamics simulation profiles $\Delta T_{B,\text{sim}}$ are propagated forward by one analysis timestep ($\Delta t = 100$ fs) using the backbone rate constants k_{BB} fit at that step. In doing so, we generate a temperature elevation profile $\Delta T_{B,\text{fit}}$ for fit data. The deviation between fit and simulation data $\Delta\Delta T_B = \Delta T_{B,\text{fit}} - \Delta T_{B,\text{sim}}$ affords a metric for quality of reconstruction, exhibiting variations that are generally below ± 10.0 K (Fig. S3). Data are presented for simulations at $T_B = 230.0$ K, with MD simulation data coarse grained over $\Delta t = 100$ fs intervals prior to analysis.

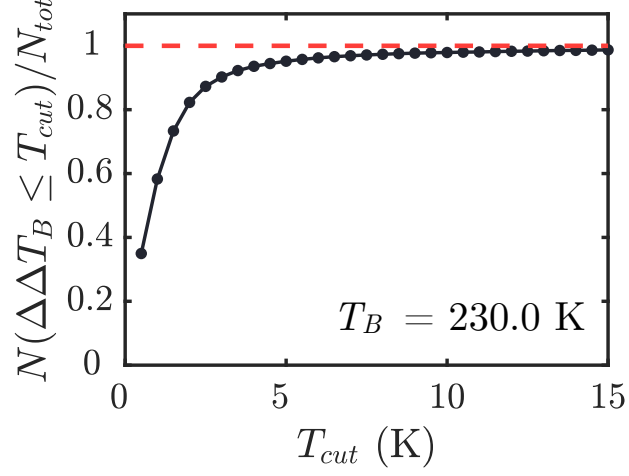


FIG. S3. **Percentage of trajectory frame deviations by temperature cutoff.** The variation between fit rate profiles and raw MD simulation (Fig. S2) may be further quantified through the percentage of trajectory propagations N/N_{tot} with a temperature deviation $\Delta\Delta T_B = \Delta T_{B,\text{fit}} - \Delta T_{B,\text{sim}}$ lying at or below a given cutoff $\Delta\Delta T_B \leq T_{\text{cut}}$ (here N_{tot} is the total number of propagations). In this case, 95.2 % of propagations exhibit a deviation of less than 5.0 K over 100 fs, while 98.0 % show a deviation of less than 10.0 K over the same time interval. At deviations up to $T_{\text{cut}} = 15.0$ K, we find that 99.0 % of propagations will lie below the cutoff. While not employed here, these values can be used to filter erroneous fits during analysis. In this case, $T_{\text{cut}} = 10.0$ K accounts for pathologies due to numerical instability while retaining robust counting statistics. Data are presented for simulations at $T_B = 230.0$, with MD simulation data coarse grained over $\Delta t = 100$ fs intervals prior to analysis.

II. CUMULATIVE HEAT TRANSFER: BATH TEMPERATURE DEPENDENCE

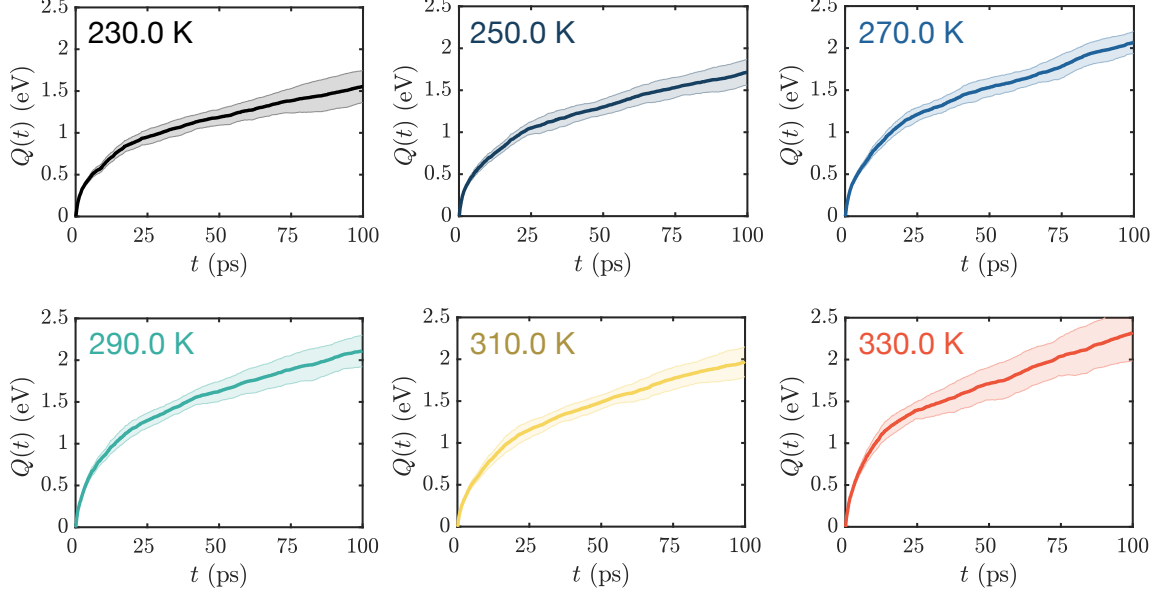


FIG. S4. **Cumulative Heat Transfer Between Residues 1 and 2.** Energy transfer is quantified by integrating the heat flux $[J_{BB}]_{i,j}$ between the i -th and j -th residues up to time t in the MD simulation trajectory: $Q(t) = \int_0^t J_{1,2}(t') dt'$. Fluxes are obtained using the master equation analysis described in the parent manuscript, with time series data coarse grained at $\Delta t = 100$ fs prior to analysis. Transfers exceed the 1.6 eV of heat added to the first residue due to residual error from short timescale transients. This behavior may be mitigated by coarse graining the trajectory over larger temporal windows, at the cost weaker statistics. The bath temperature for each trace (ΔT_B) is indicated in the upper left hand side of the plot. The error bands are plus/minus one standard error.

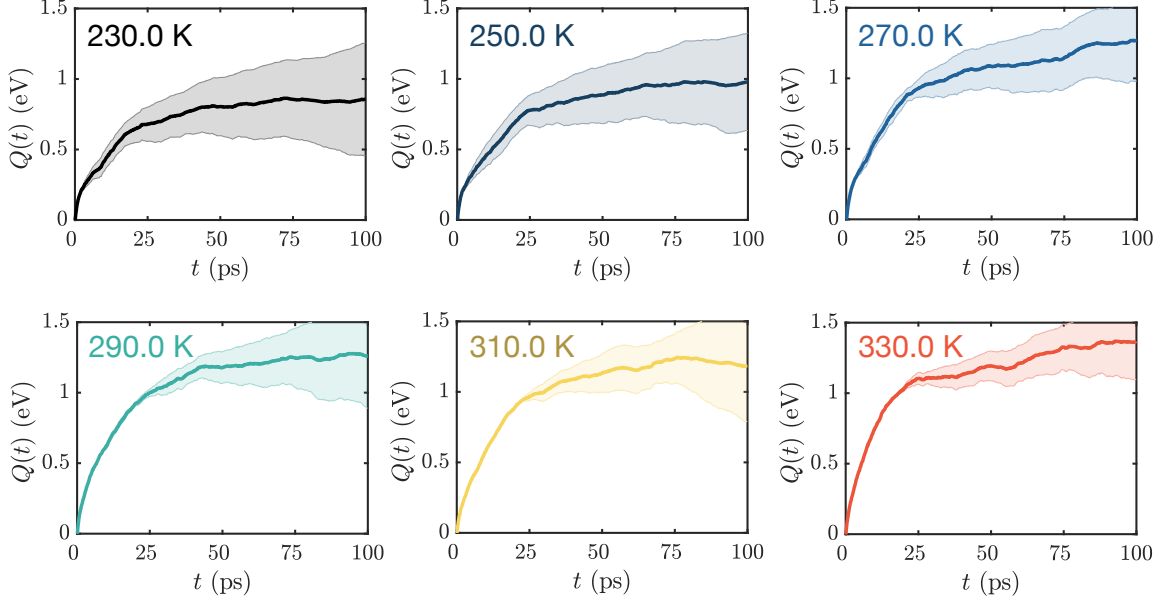


FIG. S5. **Cumulative Heat Transfer Between Residues 2 and 3.** Energy transfer is quantified by integrating the heat flux $[J_{BB}]_{i,j}$ between the i -th and j -th residues up to time t in the MD simulation trajectory: $Q(t) = \int_0^t J_{1,2}(t') dt'$. Fluxes are obtained using the master equation analysis described in the parent manuscript, with time series data coarse grained at $\Delta t = 100$ fs prior to analysis. The bath temperature for each trace (ΔT_B) is indicated in the upper left hand side of the plot. The error bands are plus/minus one standard error.

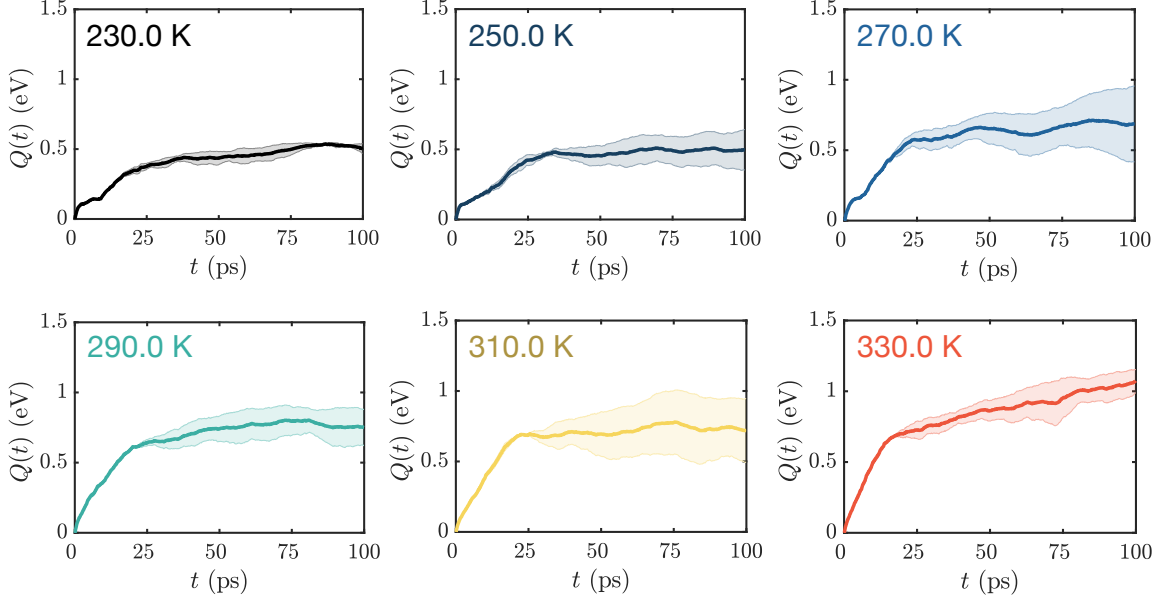


FIG. S6. **Cumulative Heat Transfer Between Residues 3 and 4.** Energy transfer is quantified by integrating the heat flux $[J_{BB}]_{i,j}$ between the i -th and j -th residues up to time t in the MD simulation trajectory: $Q(t) = \int_0^t J_{1,2}(t') dt'$. Fluxes are obtained using the master equation analysis described in the parent manuscript, with time series data coarse grained at $\Delta t = 100$ fs prior to analysis. The bath temperature for each trace (ΔT_B) is indicated in the upper left hand side of the plot. The error bands are plus/minus one standard error.

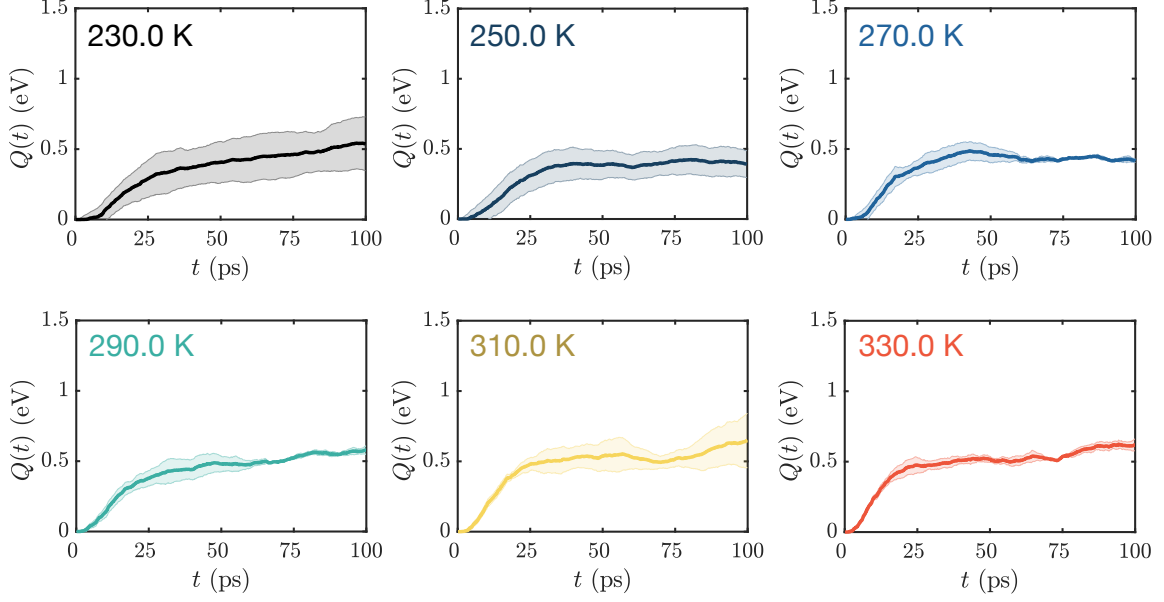


FIG. S7. **Cumulative Heat Transfer Between Residues 4 and 5.** Energy transfer is quantified by integrating the heat flux $[J_{BB}]_{i,j}$ between the i -th and j -th residues up to time t in the MD simulation trajectory: $Q(t) = \int_0^t J_{1,2}(t') dt'$. Fluxes are obtained using the master equation analysis described in the parent manuscript, with time series data coarse grained at $\Delta t = 100$ fs prior to analysis. The bath temperature for each trace (ΔT_B) is indicated in the upper left hand side of the plot. The error bands are plus/minus one standard error.

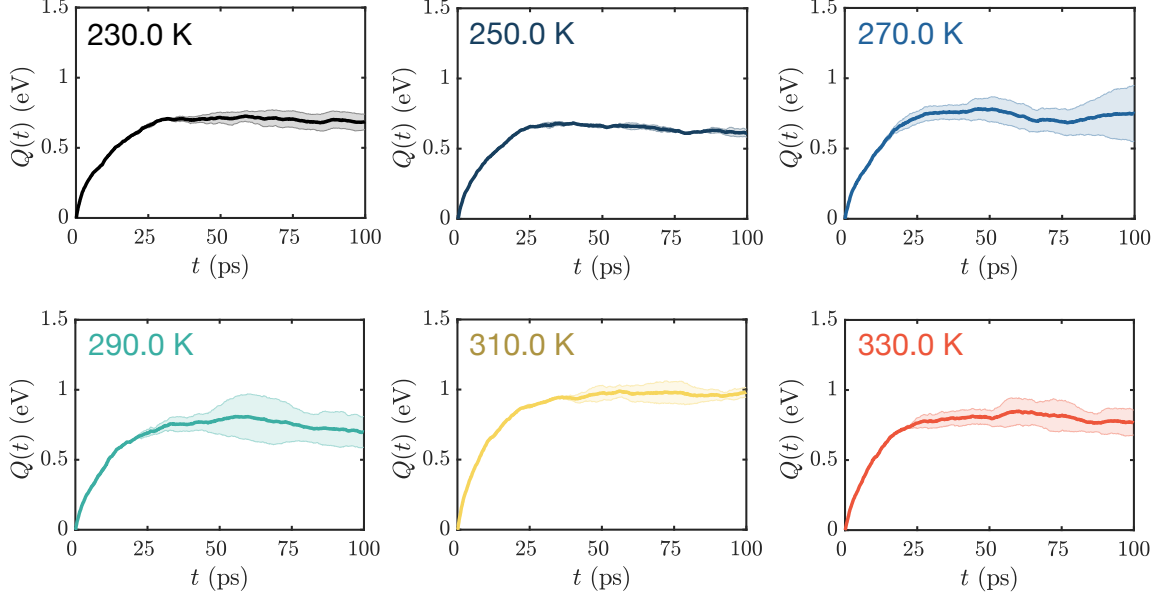


FIG. S8. **Cumulative Heat Transfer Between Residues 5 and 6.** Energy transfer is quantified by integrating the heat flux $[J_{BB}]_{i,j}$ between the i -th and j -th residues up to time t in the MD simulation trajectory: $Q(t) = \int_0^t J_{1,2}(t') dt'$. Fluxes are obtained using the master equation analysis described in the parent manuscript, with time series data coarse grained at $\Delta t = 100$ fs prior to analysis. The bath temperature for each trace (ΔT_B) is indicated in the upper left hand side of the plot. The error bands are plus/minus one standard error.

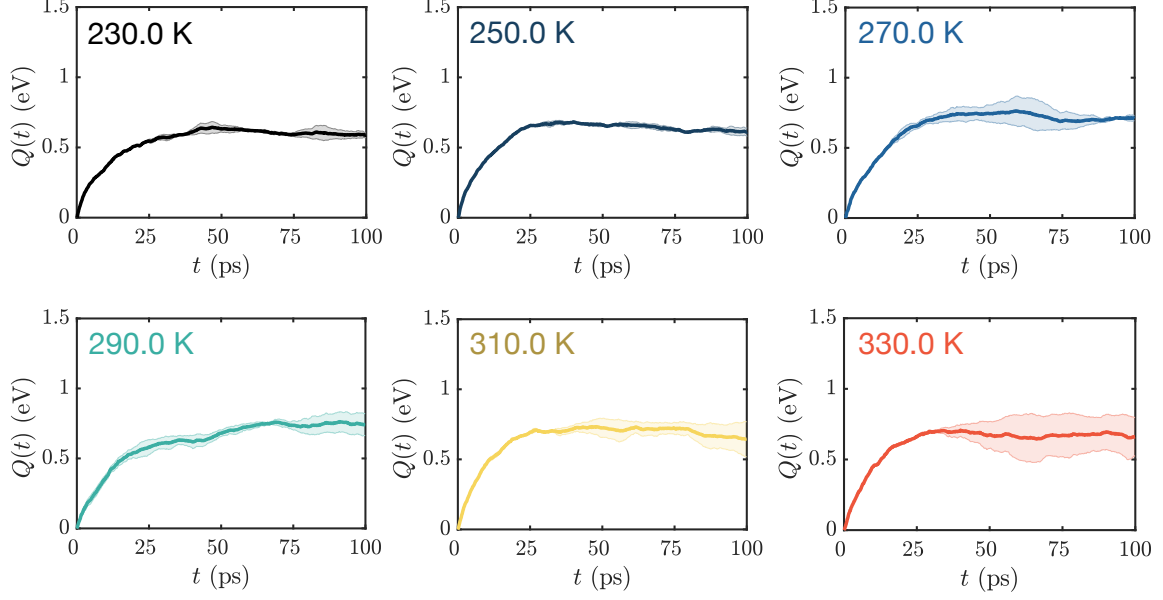


FIG. S9. **Cumulative Heat Transfer Between Residues 6 and 7.** Energy transfer is quantified by integrating the heat flux $[J_{BB}]_{i,j}$ between the i -th and j -th residues up to time t in the MD simulation trajectory: $Q(t) = \int_0^t J_{1,2}(t') dt'$. Fluxes are obtained using the master equation analysis described in the parent manuscript, with time series data coarse grained at $\Delta t = 100$ fs prior to analysis. The bath temperature for each trace (ΔT_B) is indicated in the upper left hand side of the plot. The error bands are plus/minus one standard error.

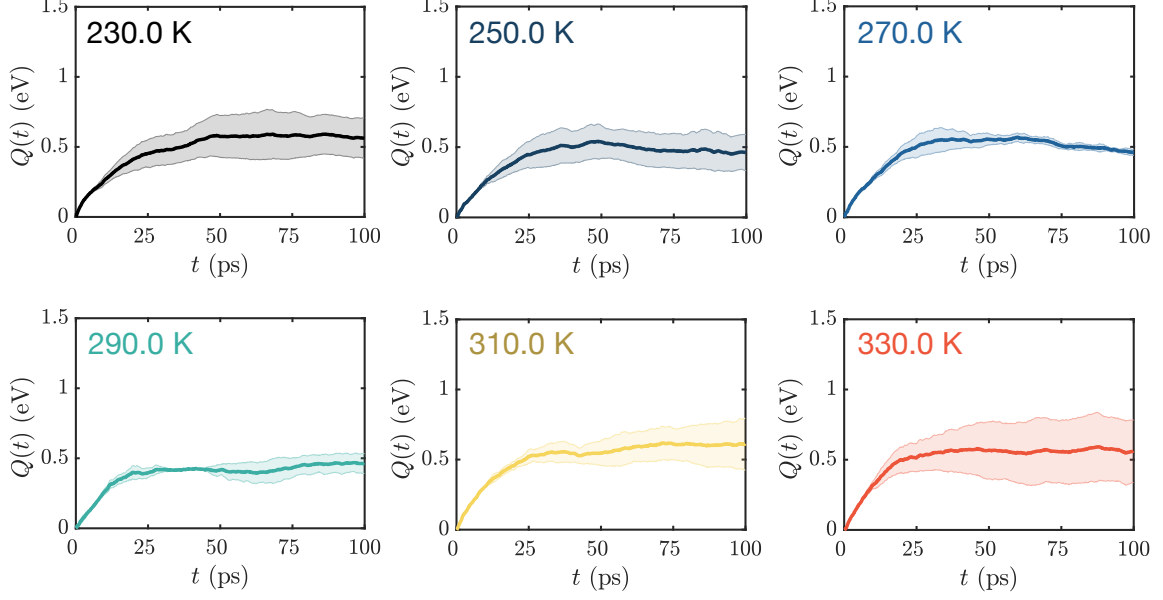


FIG. S10. **Cumulative Heat Transfer Between Residues 7 and 8.** Energy transfer is quantified by integrating the heat flux $[J_{BB}]_{i,j}$ between the i -th and j -th residues up to time t in the MD simulation trajectory: $Q(t) = \int_0^t J_{1,2}(t') dt'$. Fluxes are obtained using the master equation analysis described in the parent manuscript, with time series data coarse grained at $\Delta t = 100$ fs prior to analysis. The bath temperature for each trace (ΔT_B) is indicated in the upper left hand side of the plot. The error bands are plus/minus one standard error.

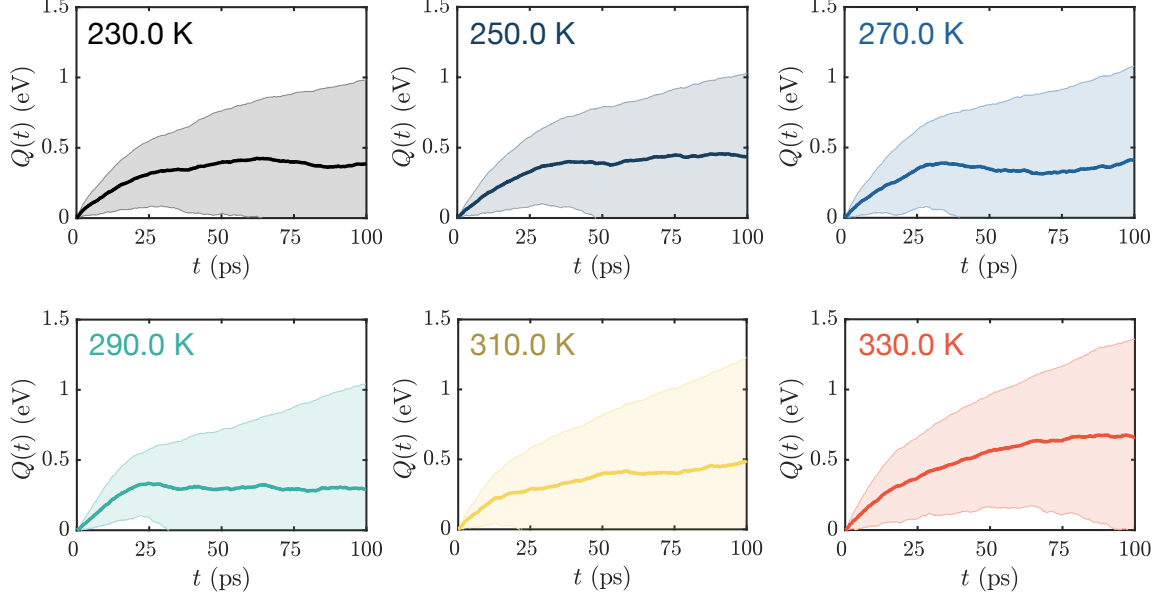


FIG. S11. **Cumulative Heat Transfer Between Residues 8 and 9.** Energy transfer is quantified by integrating the heat flux $[J_{BB}]_{i,j}$ between the i -th and j -th residues up to time t in the MD simulation trajectory: $Q(t) = \int_0^t J_{1,2}(t') dt'$. Fluxes are obtained using the master equation analysis described in the parent manuscript, with time series data coarse grained at $\Delta t = 100$ fs prior to analysis. The bath temperature for each trace (ΔT_B) is indicated in the upper left hand side of the plot. The error bands are plus/minus one standard error.

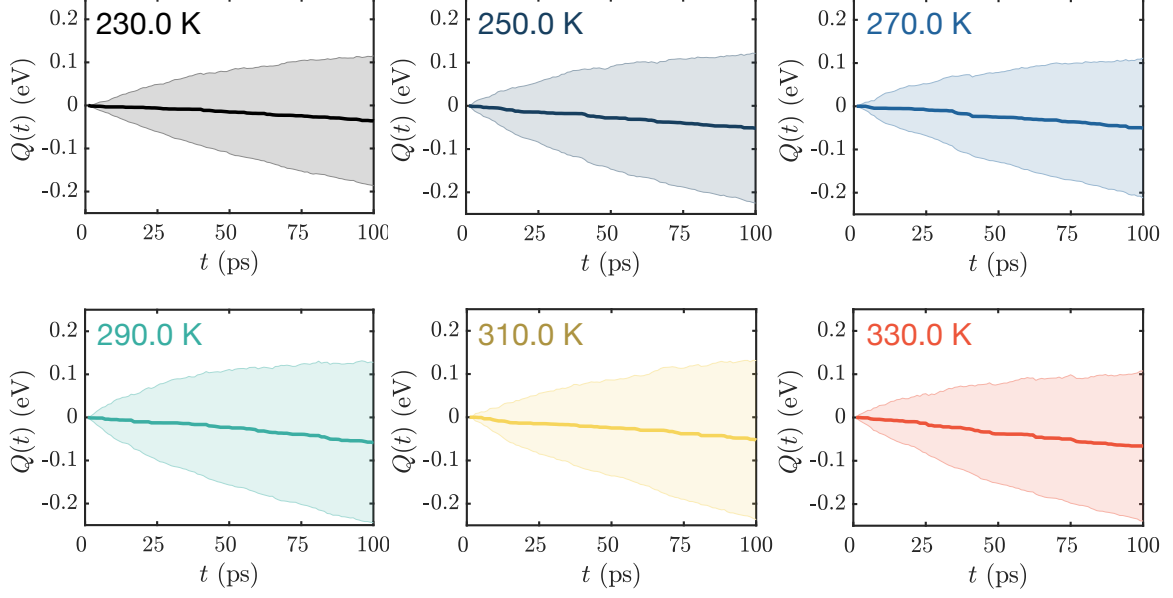


FIG. S12. **Cumulative Heat Transfer Between Residues 9 and 10.** Energy transfer is quantified by integrating the heat flux $[J_{BB}]_{i,j}$ between the i -th and j -th residues up to time t in the MD simulation trajectory: $Q(t) = \int_0^t J_{1,2}(t') dt'$. Fluxes are obtained using the master equation analysis described in the parent manuscript, with time series data coarse grained at $\Delta t = 100$ fs prior to analysis. The high flexibility of residue 10 leads to intermittent contact with the remainder of the peptide. Consequently, we observe weak heat transfer from the thermal pulse, although transient contacts do result in a small negative $Q(t)$. This corresponds to a thermal transport pathway from the solvent to residue 9, using residue 10 as an intermediary. The error bands are plus/minus one standard error.

III. HYDROGEN BOND TRANSPORT: FLUX DISTRIBUTION

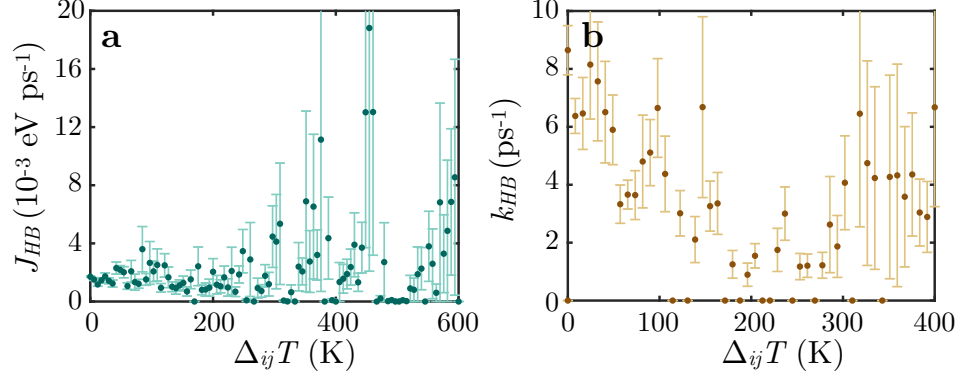


FIG. S13. **Hydrogen Bond Rates and Fluxes.** (a) Hydrogen bond flux distributions (J_{HB}) for helical Aib₁₀ conformers. Fluxes are parameterized by the effective temperature gradient $\Delta_{ij}T_{\text{eff}}$ between adjacent residues, taken as positive when $i > j$. (b) Rate constants (k_{HB}) corresponding to the hydrogen bond flux distribution. Rates and fluxes are obtained by fitting a kinetic master equation (Eq. 1 from the parent manuscript) to MD simulation data that has been coarse grained over $\Delta t = 100$ fs intervals. The resulting fluxes and rates are block averaged into 1.0 K bins. The error bars are plus/minus one standard error.

IV. DISTRIBUTION OF EFFECTIVE BACKBONE GRADIENTS ($\Delta_{ij}T_{\text{eff}}$)

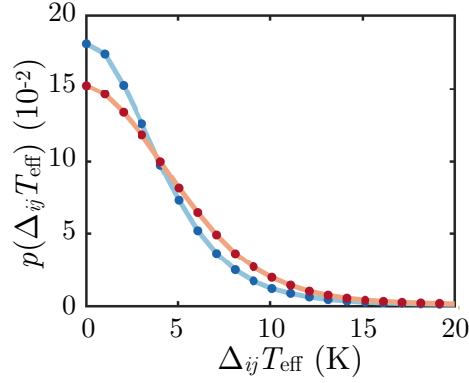


FIG. S14. **Distribution of backbone temperature gradients.** The probability density distribution $p(\Delta_{ij}T_{\text{eff}})$ for the effective temperature gradient $\Delta_{ij}T_{\text{eff}}$ between adjacent residues (taken as positive when $i > j$) is calculated directly from simulation data. Data are partitioned into low-temperature (blue; 230 K to 270 K) and high-temperature (red; 290 K to 330 K) regimes. Distributions are calculated using trajectory frames that have been coarse grained over $\Delta t = 100$ fs intervals, and are themselves averaged into 1.0 K bins.

V. HEAT DIFFUSIVITY AND MASTER EQUATION ANALYSIS

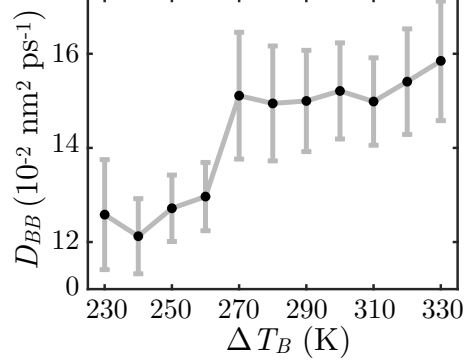


FIG. S15. **Heat diffusivities calculated from backbone rate constants.** The effective backbone heat diffusivity $D_{BB} = k_{BB} (\Delta x)^2$ may be estimated using the rate constants k_{BB} from master equation analysis. Diffusivities are calculated $D_{BB}(T_B) = \sum_{\ell=1}^N k_{BB,\ell} p_{\ell} (\overline{\Delta x})^2$ at each bath temperature T_B , where summation is over all N bins of the thermal gradient $\Delta_{ij} T_{\text{eff}}$ distribution, p_{ℓ} is the weight assigned to each bin (Fig. S14), and $\overline{\Delta x}$ is the mean residue separation. The resulting diffusivities exhibit scaling that mimics the full simulation data (Fig. 2a in the manuscript), albeit with a slightly larger magnitude. While deviations exist (particularly for $T_B = 240$ K), these likely reflect the simplified interactions accommodated by our model, alongside limitations due to sampling. The overall similarity suggests that most critical processes are captured by the master equation approach, supporting the scope of our interpretation. The error bands are plus/minus one standard error.